Paper accepted for publication in Journal of Sound and Vibration, 7 May 2020

Modelling of vibration and noise behaviour of embedded tram tracks using a wavenumber domain method

Wenjing Sun [a]*, David Thompson [b], Martin Toward [b], Zhaoran Zeng[a]

[a] *Institute of Rail Transit, Tongji University, Shanghai, 201804, People's Republic of China*;

[b]*Institute of Sound and Vibration Research, University of Southampton, Southampton SO17 1BJ, UK*

Abstract: Tracks with rails embedded in a layer of rubber are commonly used for tramways. The vibration and sound radiation behaviour of these tracks differs from that of conventional railway tracks. This is studied here using coupled wavenumber finite element and boundary element models. A detailed analysis is carried out for an embedded rail with a narrow embedding material and comparisons are made with field measurements. The rail, embedding material and surrounding concrete are modelled with finite elements, whereas the support conditions due to the underlying ground are modelled with structural boundary elements coupled to the base of the track model. The sound radiation is calculated using a wavenumber acoustic boundary element model in which it is assumed that there is only one-way coupling with the structure. At low frequencies, vibration of the concrete slab also contributes to the noise radiation. Consequently, the radiated sound is increased compared with that produced by the rail alone at low frequencies but it is reduced above 300 Hz, where the rail and concrete vibrate out of phase with one another; at frequencies above 500 Hz the concrete has negligible effect. The track decay rate has a broad minimum between 500 and 1000 Hz; the noise radiation therefore has a peak in this important frequency region. However, the decay rate increases strongly above 1000 Hz due to the influence of the embedding material. The track considered has a grass in-fill between and outside the rails and allowing for the absorptive effect of the grass leads to a small reduction in the sound radiation. In addition, the attenuation effect of the fairings around the bogie region is estimated taking account of the absorptive effect of the grass surface. The embedded rail models are coupled with a model of a tram wheel and used to

predict the rolling noise during the passage of a tram, showing good agreement with field measurements. Finally, various alternative embedded rail designs are compared, including different shapes of the embedding material and different rail profiles. Differences of up to 3 dB are found between the various designs.

Keywords: Tramway; embedded track; groove rail; rolling noise; wavenumber domain method; ground impedance.

1. Introduction

The noise from railways has received considerable attention in recent years. Engineering models for predicting the rolling noise of conventional railways, including ballasted and slab tracks, are well established [1]. In contrast, the noise and vibration from tramways has received much less attention, especially for tracks with embedded rails. Nevertheless, due to their proximity to sensitive receivers, the noise and vibration from trams can produce considerable annoyance to residents [2, 3]. Railway rolling noise is excited by the roughness of the rails and wheels [4] and previous studies have shown that the rail roughness on tramways can be as much as 20 dB higher than on typical mainline railways [5, 6]. Therefore, although the speed is low, the rolling noise can be significant. The low speed also means that the contact filter normally adopted in rolling noise models [7] needs to be extended to shorter wavelengths. Embedded rails that are commonly used on tramways can lead to an increase in radiation of the rail noise in an important part of the frequency range. Although models have been developed for studying the rolling noise from trains on open rails [8], these have not been widely applied to trams and tram tracks.

The generation and propagation of rolling noise from embedded tracks is different from conventional railways. It can be affected by various factors, such as the use of a different rail profile, the fact that the rail support is continuous rather than discrete, the geometry of the embedding material and the ground properties. Pallas et al. [9] used a microphone array to identify different sound sources on two types of tramcar running on two types of embedded track, one in the street and one in a ground covered with grass. The results showed that the rolling noise level was more affected by the track type than the vehicle type. However, the vibro-acoustic behaviour of these types of track and the reasons for the differences between them have not been investigated thoroughly in previous studies.

The filling material of embedded tracks has an important influence on both the noise and vibration of the track structure. Van Lier [10] used the TWINS model [8] to compare predictions of the rolling noise from a conventional ballasted track, a slab track with embedded rail and a novel embedded track with a small rail cross-section. Nilsson et al. [11] presented a model based on a wavenumber finite element (FE) and boundary element (BE) method and used it to compare the acoustic radiation of an open rail and an embedded groove rail for a unit force excitation. This approach (also known as 2.5D FE/BE) is more efficient than a full three-dimensional model. The results showed that the embedded track has a different sound radiation characteristic from the open rail. Zhao et al. [12] built an embedded track model with a finite length using conventional finite element and boundary element software. They also performed an optimization to minimise the noise by changing the filling block shape and stiffness.

The acoustic influence of the ground surface on railway noise generation has been considered in recent studies. Zhang et al. [13] and Ryue et al. [14] considered the influence of an absorptive ground on the sound radiated by a rail. The composition of the ground material around the track can change the boundary conditions for the noise generation and propagation, which should be taken into account in the prediction of rolling noise.

Various types of resilient wheel are normally used for tramcars, in which the tyre is resiliently mounted on the inner part of the wheel. These are generally quieter than all-steel wheels, due to their smaller diameter and higher damping as well as the presence of the resilient layer, but they can increase the sound radiation from the track. Jones and Thompson [15] established a finite element model of a resilient wheel and used it with the TWINS rolling noise model to study its sound radiation. Similarly, Bouvet et al. [16] presented an optimization of resilient wheels for rolling noise reduction. The results of these studies showed that the parameters of resilient wheels can affect the noise from the track as well as the wheel; these need to be determined carefully for noise control.

The aim of this paper is to study the noise generation from embedded track structures by establishing a suitable track noise prediction model. By using wavenumber domain models, the track model can be effectively infinite in length. Details of the track cross-section are included through finite elements and the sound radiation is calculated using acoustic boundary elements. Structural boundary elements are used for the underlying ground. This track model is then combined with a model of a resilient wheel and used to calculate the rolling noise. In Section 2, the waveguide finite element models and wavenumber domain boundary element models of the embedded track are introduced. The vibration and sound radiation from an embedded track

in grass are calculated and the influence of different parts of the track structure are investigated in Section 3; the effect of the acoustic impedance of the grass is discussed in Section 4. In Section 5, the rolling noise is predicted by combining the track model with a resilient wheel model and results are compared with field measurements. Then, based on the prediction model, different shapes of embedding material and different rail profiles are compared in Section 6 in order to provide a basis for the design of low noise embedded tracks.

2. Embedded track models

2.1 Wavenumber domain method

In this section, the waveguide finite element (2.5D FE) and wavenumber domain boundary element (2.5D BE) methods used in this study are described briefly, based on reference [11]. The track structure is considered as infinite in length in the *x*-direction with a constant cross-section. The equation of motion at frequency ω can be written as

$$\left[\mathbf{K}_2 \frac{\partial^2}{\partial x^2} + \mathbf{K}_1 \frac{\partial}{\partial x} + \mathbf{K}_0 - \omega^2 \mathbf{M}\right] \hat{\mathbf{U}} = \hat{\mathbf{F}} \tag{1}$$

where $\mathbf{K}_2$, $\mathbf{K}_1$ and $\mathbf{K}_0$ are stiffness matrices, $\mathbf{M}$ is the mass matrix of the cross-section, $\hat{\mathbf{U}}$ is the vector of displacements at the FE nodes and $\hat{\mathbf{F}}$ is the external force vector. ^ is used to indicate variables in the spatial and frequency domain.

A Fourier transform is performed from the *x* coordinate to the wavenumber domain (denoted by ~) yielding:

$$[\mathbf{K}_2(-\mathrm{i}k_x)^2 + \mathbf{K}_1(-\mathrm{i}k_x) + \mathbf{K}_0 - \omega^2 \mathbf{M}]\tilde{\mathbf{U}} = \tilde{\mathbf{F}} \tag{2}$$

where k_x is the wavenumber in the *x*-direction. The displacements in the wavenumber domain $\tilde{U}(k_x)$ can be obtained by solving this equation at each frequency and wavenumber; they can then be transformed back to the spatial domain by an inverse Fourier transform.

In addition to the 2.5D FE model, two BE domains are introduced and coupled with the FE domain. 2.5D elastodynamic boundary elements [17] are used to include the interaction between the track structure and the underlying ground, whereas 2.5D acoustic boundary elements are used to represent sound radiation into the air. The matrix equation for the solid BE model is written as follows [18]:

$$\mathbf{H}_{\text{solid}} \tilde{\mathbf{u}} = \mathbf{G}_{\text{solid}} \tilde{\mathbf{t}} + \tilde{\mathbf{b}} \tag{3}$$

where $\tilde{\mathbf{u}}$ is a vector of the displacements at the BE nodes (in three coordinate directions) and

$\tilde{\mathbf{t}}$ is a corresponding vector of the forces acting at these nodes. The vector $\tilde{\mathbf{b}}$ denotes body forces, which are neglected in the current study. To couple the FE and BE domains, the forces along the boundary elements are set equal and opposite to those acting on the finite elements and the displacements at each pair of coupled nodes are required to be equal.

The acoustic BE domain is solved by assuming one-way coupling with the solid FE domain. Since the fluid is air, and the structure has a much higher impedance, it can be assumed that the pressure from the fluid will have negligible effect on the FE model of the structure. The velocities from the WFE model are therefore considered as input boundary conditions for the BE fluid model at the coupling nodes. For a given frequency and wavenumber, the governing equation for the fluid is as follows

$$\mathbf{H}(k_n)\tilde{\mathbf{\Psi}} - \mathbf{G}(k_n)\frac{\partial\tilde{\mathbf{\Psi}}}{\partial\mathbf{n}} = 0 \tag{4}$$

where **H** and **G** are matrices of acoustic Green's functions, $\tilde{\mathbf{\Psi}}$ and $\frac{\partial\tilde{\mathbf{\Psi}}}{\partial\mathbf{n}}$ are vectors of the velocity potential and the normal velocity at the nodes of the boundary elements, **n** is the unit normal vector and k_n is the acoustic wavenumber component in the y–z plane, which satisfies $k_x^2 + k_n^2 = \omega^2/c_0^2$.

The boundary conditions of the WBE model can be established in the wavenumber domain in the form

$$c_a\tilde{p} + c_b\tilde{v}_n = c_c \tag{5}$$

where $\tilde{p}$ is the sound pressure, $\tilde{v}_n$ is the normal velocity, and c_a, c_b and c_c are coefficients specifying the boundary conditions. For example, when the fluid boundary is rigid these take the values c_a=0, c_b=1, c_c=0. For the nodes coupling the FE and BE models, c_c is instead set equal to the imposed normal velocity from the structure.

The radiated sound power can be obtained by integrating the power over the wavenumber domain. The results will also be presented as a radiation efficiency, determined according to

$$\sigma = \frac{W}{\rho_0 c_0 \Gamma\langle\overline{v^2}\rangle} \tag{6}$$

where W is the radiated sound power, $\langle\overline{v^2}\rangle$ is the mean-square velocity averaged over the perimeter Γ and integrated over the length, and $\rho_0 c_0$ is the characteristic acoustic impedance of air. The overbar ($\overline{\ }$) indicates the mean-square over time and $\langle\ \rangle$ means the average over the

surface area.

2.2 Numerical models of embedded track

The models are applied initially to an embedded tramway track from a particular tram system in which the track is surrounded by grass. Measurements have been carried out of rail roughness, wheel roughness, track mobility and track decay rate, which are used as input data for the noise prediction model and for validation purposes. The exterior noise of the tram in operation has also been measured for comparison with the prediction model.

The embedded track studied here is shown in Figure 1. The rail is a groove rail of type 59R2 which is coated with an elastomeric embedding material and then cast into concrete. The free surface of the rail head, embedding material and concrete can all radiate noise. The embedding material has an influence on both the rail vibration and the track noise radiation. Due to its absorptive effect, the grass around the track can also affect the sound pressure level at the receiver.

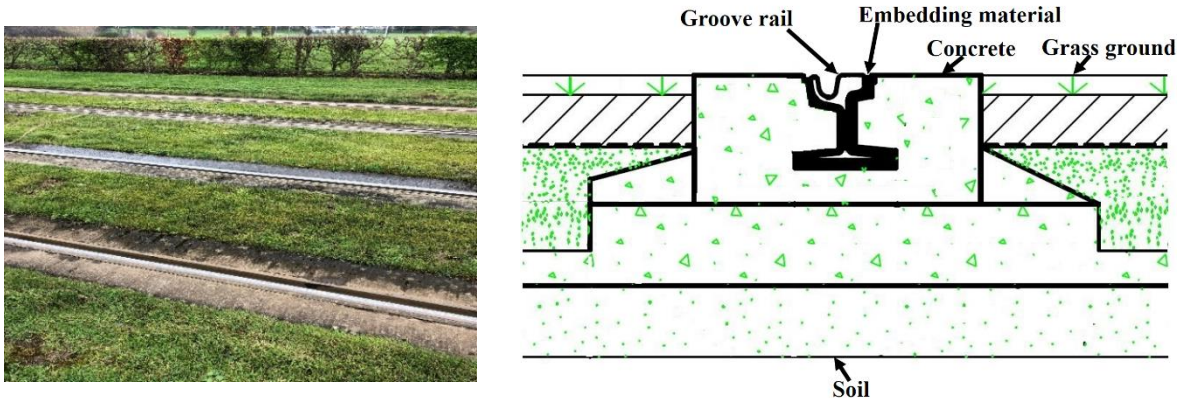

(a) (b)

Figure 1. Embedded track form of tramway: ‘grass track’. (a) Photograph; (b) cross-section.

For the embedded track structure in Figure 1, two different track vibration models are considered. In the first, the track is represented only by the groove rail and elastomer filling, as shown in Figure 2(a). The outer edges of the embedding material are constrained over all their edges apart from the upper surface; the concrete and ground material are ignored. The vibration and sound radiation from both the rail and the embedding material are taken into account. The FE mesh shown in Figure 2(a) has 216 8-noded finite elements and 1779 degrees of freedom in total. The parameters used for the embedded track model are listed in Table 1. In order to study the effect of the mass of the embedding material, the model is also run with a reduced

density of 1.5 kg/m^3 for the embedding material. Two different force positions are used, marked as F_1 and F_2 in Figure 2(a). Position F_1 is the nominal running position and is used for the calculations of vibration and noise, whereas position F_2 corresponds to the position used during impact hammer tests and is therefore used in comparison with these static measurements.

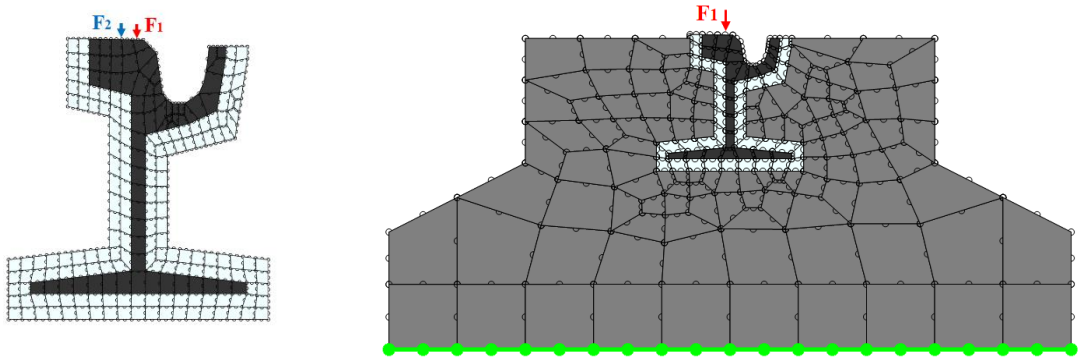

(a) (b)

Figure 2. Geometry and mesh of track vibration model. (a) Groove rail and embedding material; (b) Model with concrete and soil. Thick line with dots indicates elastodynamic boundary elements.

In the second model, shown in Figure 2(b), the surrounding concrete is also included. As it is expected that the influence of the concrete on the vibration and noise will be restricted to low frequencies, the maximum distance between nodes can be larger than in the first model. There are 174 elements and 1701 degrees of freedom in this 2.5D finite element model of the track structure. Additionally, elastodynamic boundary elements are included, based on full-space Green's functions [18], to represent the soil beneath the track and coupled with the FE model beneath the track structure, which is represented by a thick line with dots in Figure 2(b); the ground properties represent a homogeneous soil. Thus, the vibration of the concrete and the influence of the underlying soil on the rail response can be obtained with this model. The parameters used in this model are also listed in Table 1. The shear wave velocities are used to evaluate the required mesh size for all materials, especially for the embedding material and soil, so that a minimum of four nodes are included within a wavelength.

Table 1. Parameters of groove rail, embedding material, concrete and ground

Parameter	Rail	Embedding material	Concrete	Soil
Young's modulus (MPa)	211000	4.2	43000	107
Density (kg/m^3)	7850	1500	2500	1835
Poisson's ratio	0.3	0.45	0.15	0.30
Damping loss factor	0.02	0.25	0.01	0.04
Shear wave velocity (m/s)	3220	31.1	2730	150

The 2.5D acoustic boundary element model is shown in Figure 3. In this model, a half-space formulation is used to account for a ground of infinite extent. The local region close to the rail is modelled with acoustic boundary elements, allowing an absorptive surface to be included to represent the grass (see Section 4). This BE region should be large enough that the edges have negligible effect on the result; to ensure this, the BE domain representing the ground should extend at least one acoustic wavelength on each side of the rail. Moreover, the maximum distance between nodes should be less than a quarter of the acoustic wavelength. The values used are listed in Table 2. To obtain a suitable balance between calculation efficiency and accuracy, low frequency models are used up to 500 Hz and a second, smaller mesh is used for high frequencies between 500 Hz and 5000 Hz. The high frequency models are shown in Figure 3 in which only part of the FE domain is shown. When the concrete is included in the FE model its vibration is coupled to the BE mesh (Figure 3(a)) whereas in the model without the concrete this region is given a velocity of zero in the BE model (Figure 3(b)). With these 2.5D BE models, the sound radiation from the embedded track can be evaluated due to the vibration determined with the FE model.

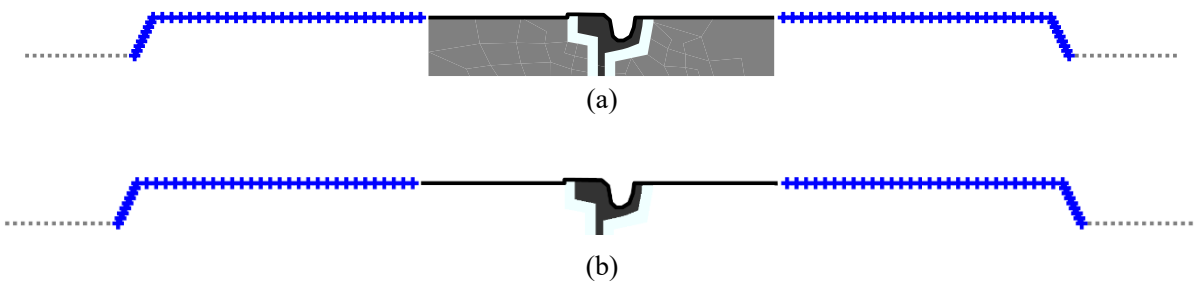

(a)

(b)

Figure 3. WBE acoustic model of embedded track showing coupling with WFE model (high frequency mesh). (a) model with concrete; (b) model of groove rail and embedding material model

without concrete. The thick black line indicates the profile of rail, embedding and concrete exposed to the air; the FE and BE models are coupled on this line but nodes are omitted for clarity. The crosses are the nodes on the acoustic BE where an impedance boundary is included. The grey dots represent the infinite boundary which is included via a half-space formulation.

Table 2. Boundary element fluid model boundary length and element size

Model	Frequency (Hz)	Acoustic wavelength (m)	Required maximum distance between nodes (m)	Length of BE domain on each side (m)	Maximum distance between nodes in BE mesh (m)
1	31.5	10.9	2.72	11	0.160
	500	0.686	0.172		
2	500	0.686	0.172	0.8	0.016
	5000	0.0686	0.0172		

3. Vibration and noise radiation of embedded track

3.1 *Dispersion curve*

For the first FE model in Figure 2(a), with groove rail and embedding material only, dispersion curves are plotted according to the eigenvectors of the finite element model. These are calculated from equation (2) with $\tilde{\mathbf{F}} = \mathbf{0}$ and the damping set to zero. The results are shown in Figure 4(a) for the model with reduced density filling and in Figure 4(b) for the normal density. The solid line in each case is the wavenumber of acoustic waves in air. Sound is only radiated to the far field when the wavenumber k_x is smaller than the wavenumber in air; this is therefore used to determine the wavenumber range for the acoustic calculations. The vibration of the rail is also sufficiently captured by this wavenumber range, as seen in Figure 4(a), but the vibration of the filling material includes waves with larger wavenumbers above 800 Hz. Nevertheless, for excitation on the rail, these short wavelength waves are not significantly excited. There are seven waves in the rail in the frequency range up to 3 kHz: vertical bending, lateral bending, torsional, web-bending, cross-section bending, foot-flapping and longitudinal waves. The same waves are also present in the case with the normal density embedding material as shown in Figure 4(b). However, above 800 Hz there are also many waves in the embedding material in this case which makes it more difficult to identify the waves in the rail. The deformation shapes of all the waves in the rail, except for the longitudinal

wave, are shown in Figure 5 for the reduced mass model.

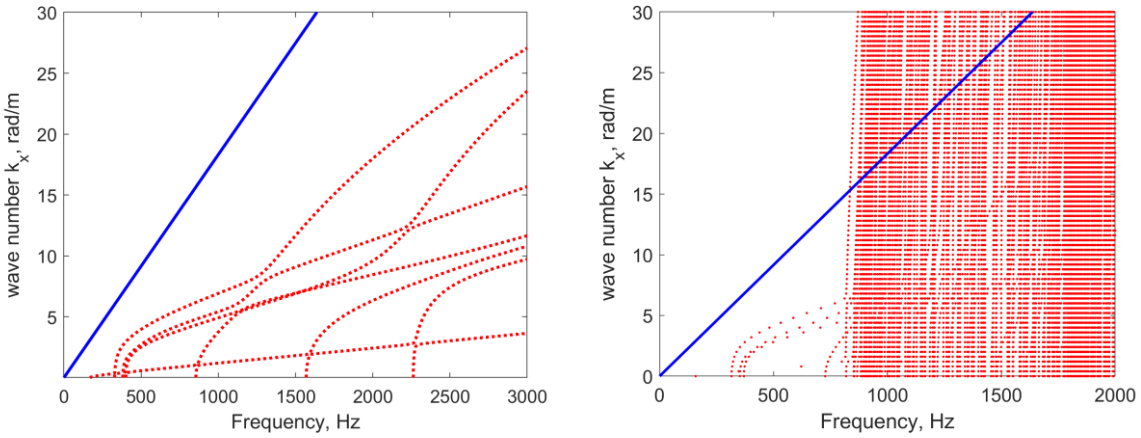

Figure 4. Dispersion curve of embedded track structure without concrete. (a) Reduced density embedding material; (b) Normal density embedding material. The solid line is the dispersion curve of acoustic waves in air.

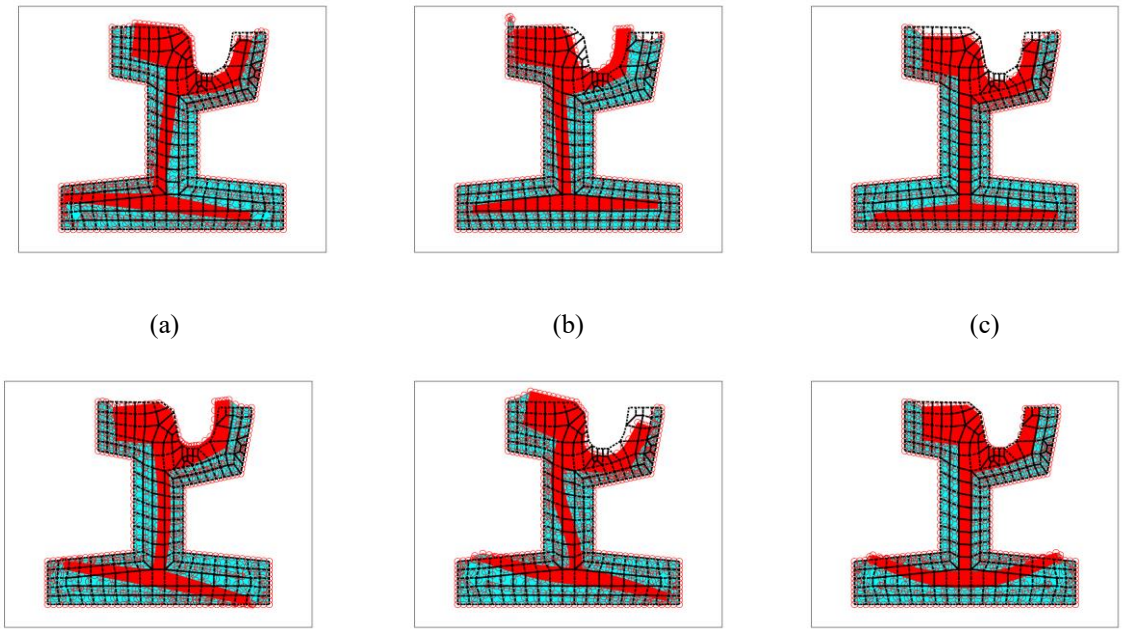

Figure 5. Wave shapes of embedded rail; (a) torsion wave at 448 Hz and wavenumber 3.5 rad/m; (a) lateral bending wave at 727 Hz and wavenumber 4.2 rad/m ; (c) vertical bending wave at 848 Hz and wavenumber 4.3 rad/m ; (d) web bending wave at 1033 Hz and wavenumber 4.2 rad/m; (e) cross-section bending wave at 1757 Hz and wavenumber 4.6 rad/m; (f) foot flapping wave at 2318 Hz and wavenumber 4.7 rad/m.

3.2 Mobility and track decay rates

A unit vertical force is applied to the rail head to obtain the vertical point mobility of the rail with 1/12 octave band frequency resolution. A maximum wavenumber of 75 rad/m is used for all frequencies, although the point mobilities are found to be almost unchanged if this range is limited to the acoustic wavenumber. The results from the models with reduced density embedding material, normal embedding material and including the concrete are shown in Figure 6(a) for the nominal force position F_1. When the concrete and ground are included, the rail mobility is increased below 100 Hz but at higher frequencies the models give similar results. Thus the model including the concrete is only used for frequencies up to 1000 Hz as the size of this model would become prohibitive at higher frequencies.

The peak at around 350 Hz corresponds to the resonance of the mass of the rail bouncing on the support stiffness, which is also the cut-on frequency of vertical bending waves in the rail, seen in Figure 4. Below this frequency the mobility is stiffness-controlled; the track support stiffness is greater than on a conventional railway for which the first peak occurs typically around 100 Hz for an unloaded track [1]. A peak appears at about 2 kHz which is due to the cut on of the foot flapping wave mode. The results for force position F_2 from the model without the concrete are compared with the measurement results in Figure 6(b). The mobility at this position is higher than at F_1 due to rotation of the rail cross-section and the peak at 2 kHz is less visible. Good agreement with the measurements is observed.

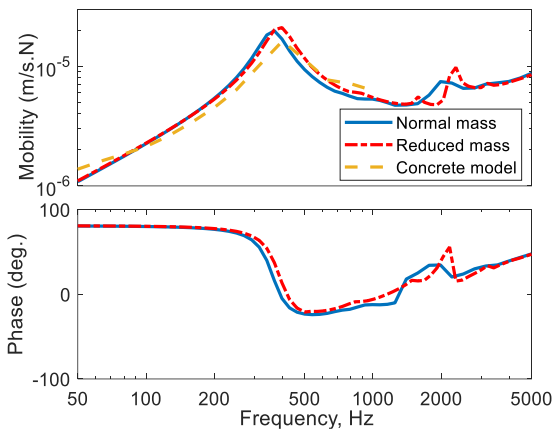

(a)

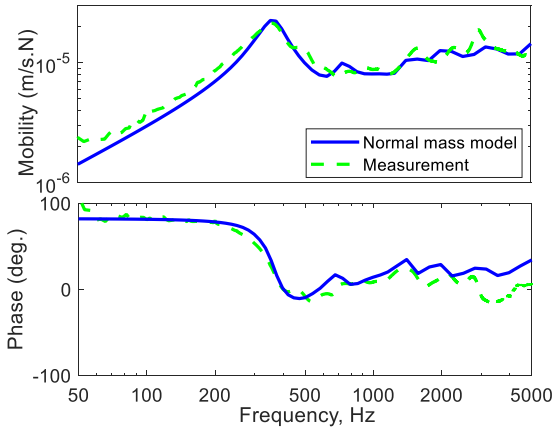

(b)

Figure 6. Mobility magnitude and phase of rail from embedded tracks in Figure 2. (a) Calculation result of different models for force position F_1. (b) Comparison between measurement results and calculation for groove rail and embedding material for force position F_2.

The track decay rate was measured in the field according to the standard EN 15461 [19]. The same method has been used with calculated responses at different positions along the rail to obtain the track decay rate from the model. As this method for determining the decay rate depends on the point mobility, results are obtained for both force positions.

The calculated vertical track decay rate for excitation point F_2 is compared with the measurements in Figure 7(a), showing good agreement. The reference curve from ISO 3095 [20] is also shown for comparison. At low frequencies, the decay rate is greater than 10 dB/m due to the blocking effect of the support stiffness [1]. It drops at around 350 Hz, which corresponds to the resonance frequency of the rail mass bouncing on the support stiffness of the filling material, seen as the peak in Figure 6. Above 1000 Hz, the track decay rate increases considerably due to the damping effect of the embedding material around the rail profile. Between these two frequencies it has a minimum.

Figure 7(b) shows the vertical track decay rates from the different track models for the nominal force position F_1. Above 400 Hz the track decay rate of the model including the concrete is slightly higher than that of the model with only rail and embedding material. Neglecting the mass of the embedding material leads to much lower decay rates at high frequencies, showing that it is important to include this mass to take account of the interaction between the rail and the embedding material [11]. A peak appears in the decay rate at 2 kHz, which coincides with the peak in the point mobility for force position F_1, i.e. due to the cut-on of the foot flapping wave. (According to the method in [19] the track decay rate is proportional to the point mobility divided by a weighted sum over transfer mobilities).

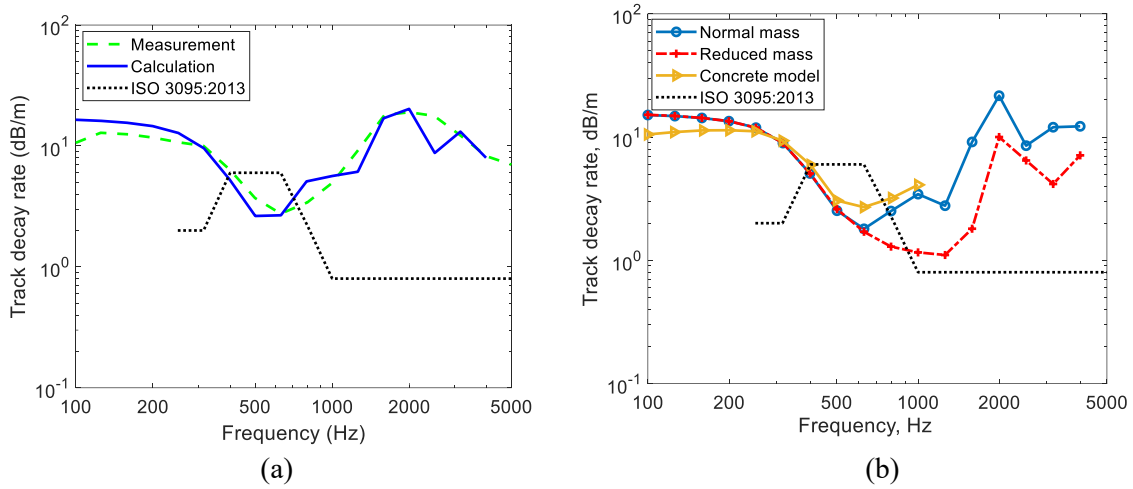

Figure 7. Vertical track decay rates in one-third octave bands. (a) Comparison between calculation for rail and embedding material only and measurement with excitation point at F_2; (b) Calculation results of different models with excitation point at wheel/rail contact point, F_1.

3.3 Radiated sound power

The radiated sound power for a unit force and the radiation efficiency are shown in Figure 8 for the various models of the embedded rail. For the models with only the rail and embedding material (Figure 2(a)) results are shown for both the normal mass model and the one with reduced density. At frequencies above 800 Hz, the sound power is higher for the reduced mass model than for the normal mass model due mainly to the difference in track decay rates (Figure 7(b)). Moreover, above 800 Hz, the radiation efficiency of the reduced mass model is also greater than that of the normal mass model.

At low frequencies, the radiation efficiency from these models increases in proportion to the frequency between about 160 Hz and 1000 Hz, corresponding to a line monopole source. This is in contrast to an open rail which acts as a line dipole, with a radiation efficiency that is proportional to the cube of the frequency [11]. Below 160 Hz the slope changes to the square of the frequency, corresponding to a point monopole; at these low frequencies the vibration of the rail is localised around the excitation point due to the high decay rate and this vibrating region becomes much shorter than the acoustic wavelength in air. Above 1000 Hz the radiation efficiency reaches unity as the width of the rail and embedding becomes comparable with half the acoustic wavelength.

Figure 8 also shows the radiated power and radiation efficiency of the model including

the concrete and ground support. In this case the result shown is actually an 'effective radiation efficiency' that is normalised with respect to the velocity and area of the rail and embedding material only, so that a higher value is found when the vibration of the concrete amplifies the sound radiation.

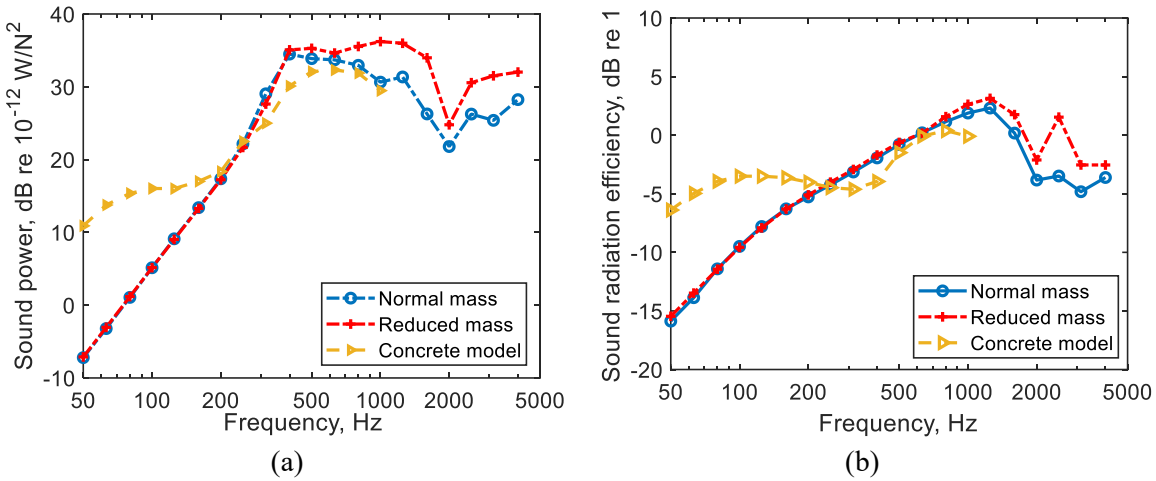

Figure 8. Sound radiation from embedded track for unit force excitation. (a) Sound power; (b) radiation efficiency.

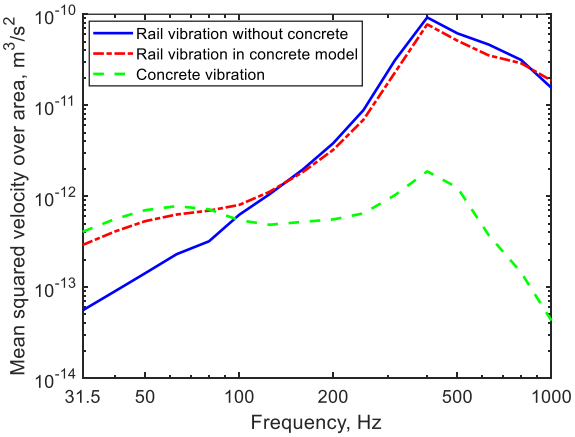

Figure 9. Mean square velocity of upper surfaces of the rail and the concrete in two models.

To show the influence of the vibration of the concrete, Figure 9 shows the mean-square velocity integrated over the surface for the models with and without the concrete. It can be seen that, above around 100 Hz, the mean-square velocities of the rail in both models are equal. Below 100 Hz, however, the vibration of both the rail and the concrete in the model including the concrete is larger than the rail vibration in the model with only the embedding material. At higher frequencies the vibration of the concrete becomes much smaller than that of the rail due

to the isolating effect of the embedding material.

As a result of the vibration of the concrete, there are differences in the sound radiation behaviour in Figure 8 at frequencies below 500 Hz. At low frequency, below 200 Hz, the sound power and radiation efficiency are greater for the model with the concrete than without due to the strong vibration of the concrete; consequently, the radiating area is greater than for the rail alone. In the region around 400 Hz, however, the sound power and radiation efficiency are lower than for the model with only the rail; in this frequency region, above the resonance peak at 350 Hz in Figure 6, the rail and concrete are vibrating out of phase with each other, leading to some cancellation of their sound radiation. Although, as seen in Figure 9, the squared velocity of the concrete is more than 50 times smaller than the rail at 400 Hz, its width is about six times larger than the rail. The width appears in the expression for the sound power twice (once in the radiation efficiency for a line monopole and once in the radiating area), giving a factor of about 36. Moreover, the length of concrete that is vibrating is greater than the corresponding length of rail.

There is a dip at 2 kHz in the sound power for a unit force. At this frequency there is a peak in the vertical mobility due to the cut-on of the foot flapping wave. As this wave has a high decay rate near the cut-on frequency, it does not contribute significantly to the radiated power, so the power shows a dip when normalized by the squared force.

4 Influence of the ground impedance

The tram track studied here is laid in a grass surface, as seen in Figure 1. This will have different acoustic properties from a ballasted track or a conventional slab track. The grass will have an absorptive effect on the rolling noise, which is taken into account in the model in this Section. For simplicity, the conventional Delany and Bazley model [21] for an infinite layer of porous material is used here to estimate the acoustic impedance, based on an equivalent flow resistivity. This impedance is included in the BE model on the ground surface. It has been found that, even if a finite thickness model is used, the impedance results are virtually unaffected.

For the equivalent flow resistivity, a value of 300 kPa.s/m^2 [22] is used to represent the grass in the BE model. In addition, a smaller value of 30 kPa.s/m^2 is used for comparison. The influence of grass ground on the sound radiation efficiency for the model with groove rail and

embedding material is shown in Figure 10(a). The absorptive properties of the grass ground (300 kPa.s/m^2) reduce the sound power over the whole frequency range by less than 1 dB. Even using the lower value of flow resistivity, the effect is less than 2 dB. Thus, including the absorptive properties of the ground has only a small effect on the sound radiation of the embedded track. Figure 10(b) shows the influence for the model with concrete; a similar effect is seen as for the model without concrete.

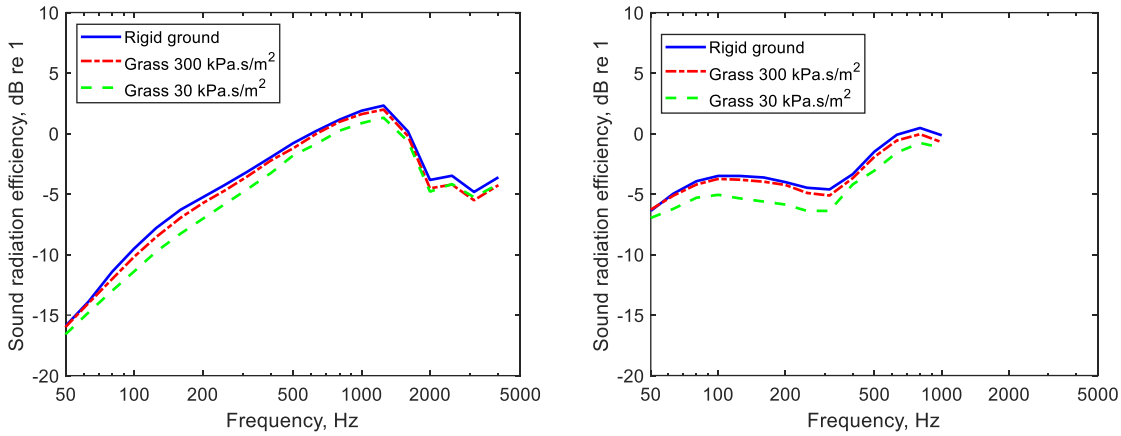

Figure 10. The influence of the ground impedance on the radiation efficiency of the embedded rail. (a) Groove rail with embedding material; (b) model with concrete.

5. Rolling noise from tram running on embedded track

5.1 *Prediction model*

Having established models for the embedded 'grass track' shown in Figure 1, the rolling noise of a tram running on this embedded track is calculated by combining these models with a resilient wheel. The relative contributions of the noise radiated by the track and the wheels can then be identified. The 2.5D FE/BE models of the track with both rigid ground surface and grass surface are used. The resilient wheel is represented by a finite element model, which has been validated with simple modal measurements on the wheels of the tram. The total length of the tram is 54 m, and the number of wheelsets is 10. The wheel radius is 0.295 m and the wheel load is assumed to be 40 kN. The noise measurement location is at 7.5 m from the track centreline and 1.2 m above the top of the rail.

Figure 11(a) shows measured wheel and rail roughness spectra from the trams and the test site. The reference curve from ISO 3095:2013 [20] is also shown for comparison. The rail

roughness of the tramway track is quite high over the whole wavelength range, as found in previous studies [5, 6]; the maximum difference with the ISO reference curve is more than 20 dB. There is no strong peak in the roughness spectra although some short wavelength corrugation was visible at a wavelength of around 20 mm. Compared with the rail roughness, the wheel roughness level is much lower.

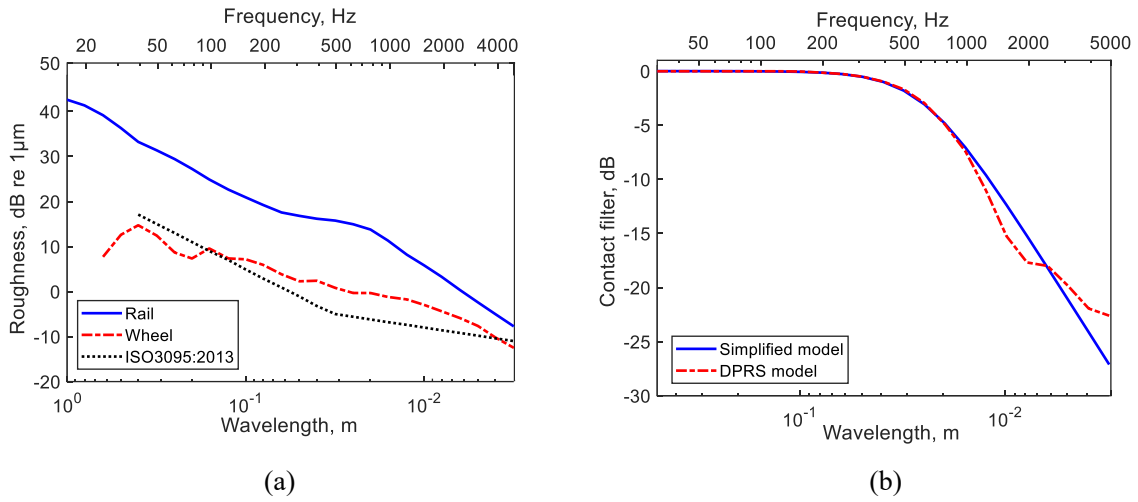

(a) (b)

Figure 11. Excitation of wheel/rail system. (a) Rail roughness of tram track and wheel roughness; (b) Contact filter effect. Frequency axis corresponds to a speed of 56 km/h.

Due to the low speed of the tram, the contact filter is particularly important. Assuming Hertzian contact, the contact area between the wheel and rail is elliptical with semi-axis lengths a and b. Roughness wavelengths shorter than the contact patch length $2a$ tend to be attenuated. Here, data from the DPRS model [1, 7] were used to obtain the contact filter effect. The contact patch length used here should be selected according to the wheel load, wheel diameter and running speed. This leads to a contact patch semi-axis length of 4.3 mm. The contact filter effect from the DPRS model is compared with the results of a simplified equation (Remington formula [1]) in Figure 11(b). For these parameters the DPRS result is lower than the simplified equation around 1.6 kHz and higher than it above 3 kHz.

In predicting the radiated noise from the embedded rail, it is assumed that the lateral vibration of the rail can be neglected as it does not radiate significantly. However, the lateral vibration of the wheel is much more important for the sound radiation. To calculate this, the wheel/rail interaction in both vertical and lateral directions must be taken into account [23].

Figure 12 shows the vertical and lateral point mobilities of the embedded track at the nominal contact point, as well as the resilient wheel and the wheel/rail contact zone. The vertical wheel mobility contains a broad peak around 100 Hz and a sharper peak at 900 Hz. The latter corresponds to a 1-nodal-diameter radial mode. At higher frequencies, there are several more wheel modes, resulting in an increase in the response of the wheel and a corresponding rise in its radiated sound.

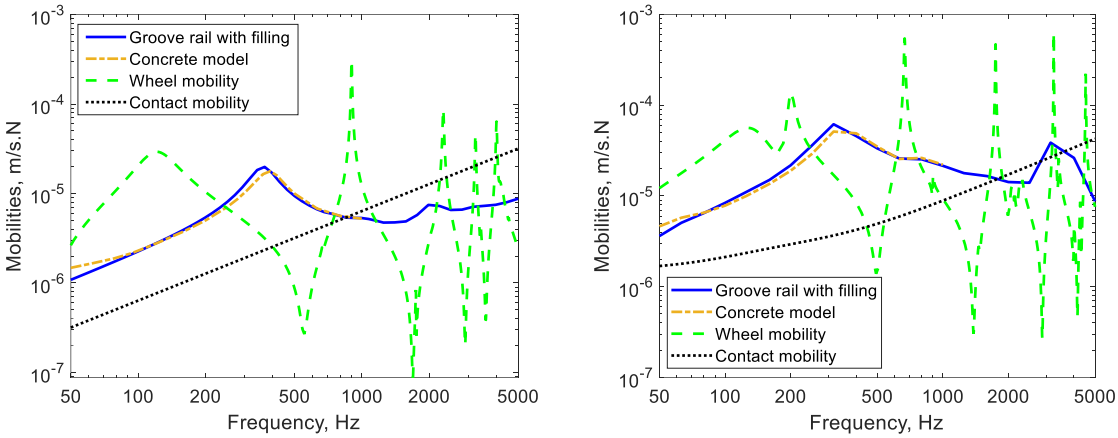

Figure 12. Mobility magnitude of rail, wheel and contact zone. (a) Vertical; (b) lateral.

The sound power and radiation efficiency of the track structure for a unit force are calculated as in Sections 3 and 4. The sound pressure level from the wheel is obtained from the TWINS model [1] using the rail mobilities from the 2.5D model to determine the wheel/rail force. These wheel and track components are then combined to determine the total rolling noise.

As well as the effect of the acoustic absorption of the grass on the radiated sound power of the track, considered in Section 4, account is taken of the fact that the track and wheels radiate into a cavity beneath the tram, shown in Figure 13(a), which contains the absorption of the grass. As in Section 4, the Delany and Bazley model [21] is used with a flow resistivity of 300 kPa.s/m^2. The diffuse field absorption coefficient is derived from the impedance using Paris's formula [24].

As the bogie cavity includes side skirts, see Figure 13(a), it is assumed that all the noise radiated from the wheels and rails is transmitted through the cavity before being radiated to the wayside. It is assumed that the cavity contains an absorption area S_{ab} (absorption coefficient multiplied by surface area) of the grass and any other absorptive surfaces and an aperture area

S_{ap} corresponding to the gap between tram car skirt and the ground. The insertion loss of this bogie cavity can be obtained as follows [25]

$$\mathrm{IL} = 10\log_{10}\left(\frac{S_{ab}+S_{ap}}{S_{ap}}\right) \tag{7}$$

Figure 13(b) shows the insertion loss of the bogie cavity obtained with a gap height of 205 mm and a total width of grass of 1.2 m. The wheel/rail noise is reduced by this insertion loss to get the sound pressure level at the receiver. The result is also shown for the lower value of flow resistivity for comparison.

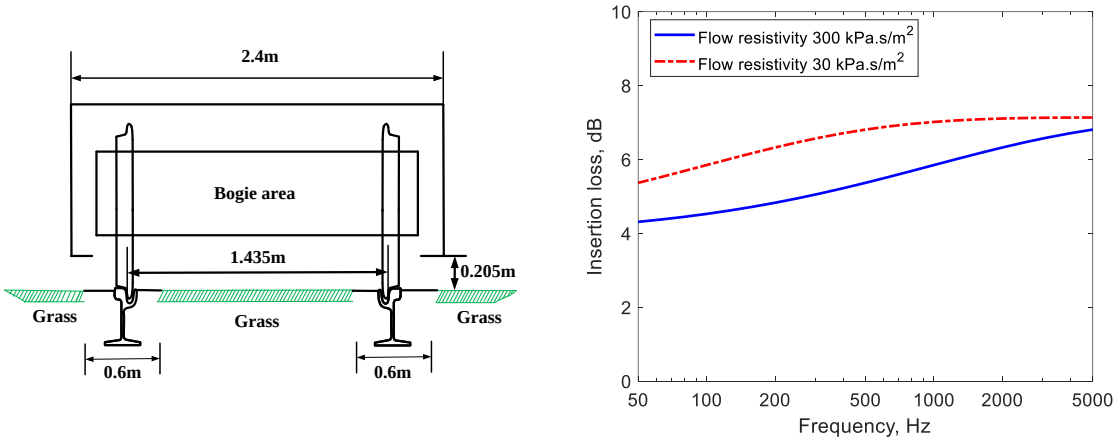

(a) (b)

Figure 13. The influence of tramcar bogie cavity. (a) Schematic cross-section view of bogie cavity; (b) insertion loss of bogie cavity.

Figure 14(a) shows the A-weighted track noise component obtained using models of the track based on the rail and filling alone and the model with the concrete, in both cases including the grass. For the latter model, the corresponding model without the concrete is used above 1 kHz. The insertion loss from Figure 13(b) is applied in each case. The main differences in the track noise between the different models come from the effects on the sound radiation seen in Figures 8 and 10. Below 200 Hz, the noise from the model including the concrete is much greater than that from the model with just the rail and embedding material; at higher frequencies, due to the acoustic cancellation between the rail and the concrete, observed in the results of Figure 8, the results for this model are slightly lower than the model based on the rail and filling alone.

The wheel/rail interaction forces (not shown here) are found to be similar for the various

models of the track. Consequently, the wheel contribution also does not differ much between the two track models, with overall levels of 69.3 dB(A) and 69.7 dB(A), the differences occurring due to small differences in the rail mobility. The total noise including the wheel and track components is shown in Figure 14(b), which shows similar trends to the track noise. The radiated noise from the track is found to have a much larger influence on the total noise than the wheel.

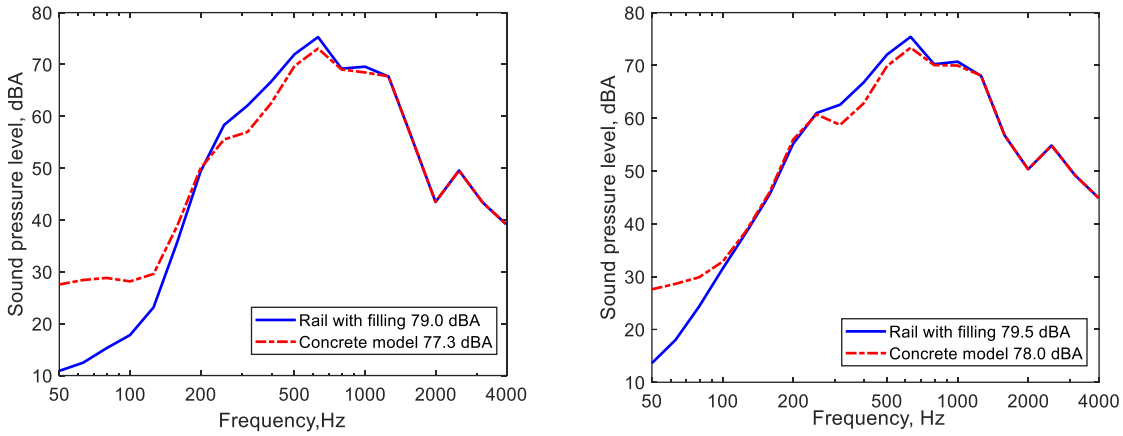

Figure 14. A-weighted sound pressure spectra calculated using different track models. (a) Track noise component; (b) total noise.

5.2 *Comparison with measurements*

Noise measurements were taken during the passage of trams. Figure 15(a) shows the measured noise from three trams with speeds of 56±1 km/h. These results are compared with the rolling noise predicted using the model with the concrete and including the impedance of the grass. Good agreement is observed over most of the frequency range. Because of the presence of background noise and noise from the equipment on the tram, the measurement is greater than the prediction, especially at low frequencies. At high frequencies the differences may be caused by inadequacies in the model of the bogie cavity screening or the contact filter. Figure 15(b) shows the wheel and track components of noise as well as the total noise spectrum. The overall contribution of the track is 7.6 dB(A) greater than that of the wheel and is dominant for frequencies between 315 and 1600 Hz. The wheel noise contribution is larger between 100 and 200 Hz and above 2000 Hz.

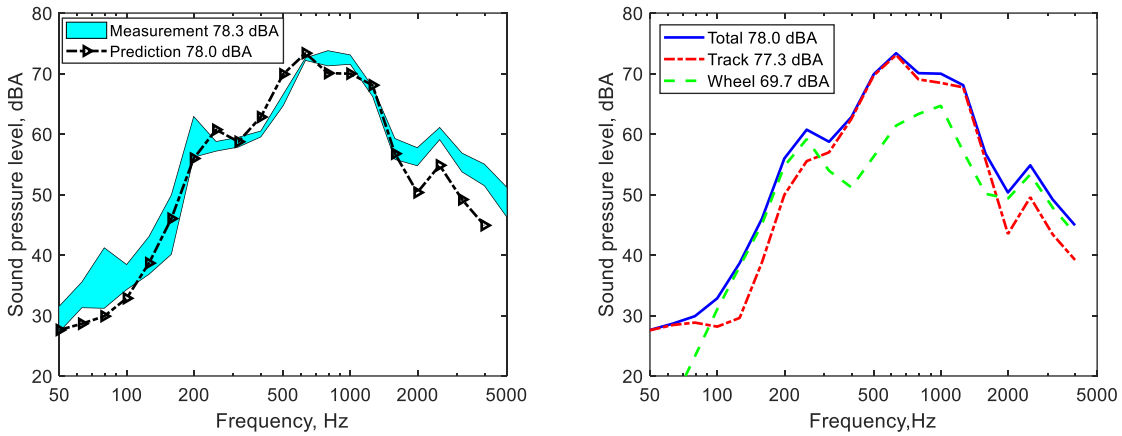

Figure 15. Rolling noise for embedded rail in concrete on grass ground; (a) Comparison of prediction and measured noise; (b) contributions to the predicted noise from wheel and track.

6. Rolling noise of embedded tracks with different rail and filling shapes

6.1 *Track models and dynamic properties of different rails and filling shapes*

Having established a model for the embedded track based on the 2.5D FE/BE method and validated it using field measurements, in this section the effects of varying the rail section and the shape of the embedding material are explored. In addition to the model with narrow embedding material considered above, four models with a wider embedding are considered, as shown in Figure 16. For the purpose of the comparison in this section, in each of these models the sound power is calculated assuming that the ground surface is rigid and the effect of the vibration of the concrete is neglected. However, the same insertion loss of the bogie cavity is considered in calculating the sound pressure level at the receiver position.

Three of these models have the same rail type as in the above model, i.e. 59R2 groove rail, but with a wider filling. The Young's modulus of the filling material is 20 MPa [11], which is stiffer than for the narrow shape and ensures the different tracks have a similar vertical stiffness. A configuration is shown in Figure 16(b) containing two PVC pipes, which are commonly used to reduce the amount of elastomeric filling material required. In Figure 16(c) a variant is included that contains a soft rail pad under the rail, used for improved ground vibration isolation. Finally, an embedded track with a Vignole rail, type 55E1, is shown in Figure 16(d). As this rail section has a narrower foot, the embedding material is also narrower; it is 10 mm wider than the foot, as for the groove rail.

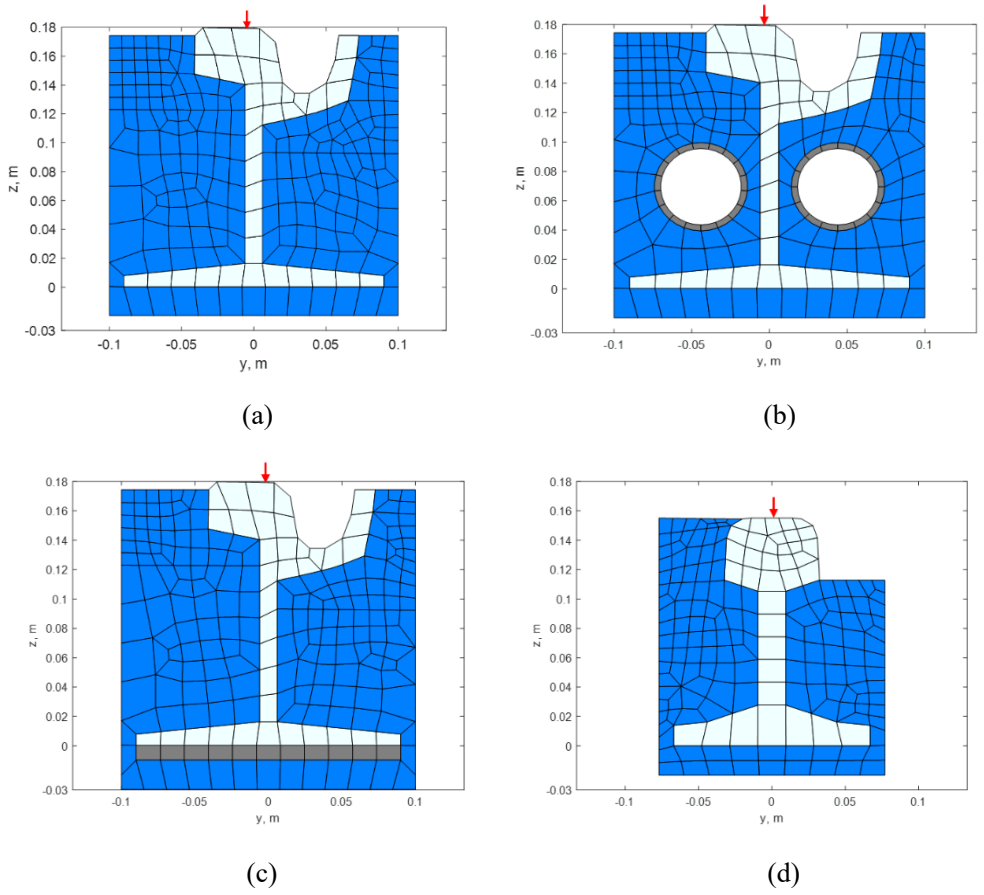

Figure 16. Geometry and mesh models of embedded tracks. (a) Groove rail with wide filling; (b) Groove rail with wide filling and PVC pipe; (c) Groove rail with wide filling and rail pad; (d) Vignole rail with wide filling.

The point mobilities and track decay rates of the different track models are shown in Figure 17. The groove rail with the narrow filling has a slightly higher resonance frequency than the others, as it has a slightly stiffer support. Conversely, the model with the soft rail pad has a higher mobility at low frequencies and a lower resonance frequency. It also has a slightly lower track decay rate in the low frequency region due to the flexibility of the rail pad. However, above 500 Hz, where the embedding has more effect than the support stiffness, it has a similar track decay rate to the corresponding model without the rail pad. At high frequencies the mobility is determined in each case by the rail bending behaviour, so the Vignole rail has a lower mobility than the more flexible groove rail.

It can be seen from Figure 17(b) that the models with the wide filling have a much higher track decay rate than the narrow one between 500 and 1600 Hz. However, the Vignole rail model has a lower track decay rate than the corresponding groove rail model above 400 Hz,

from which it can be concluded that the embedding material has a smaller influence on the Vignole rail than on the more flexible groove rail.

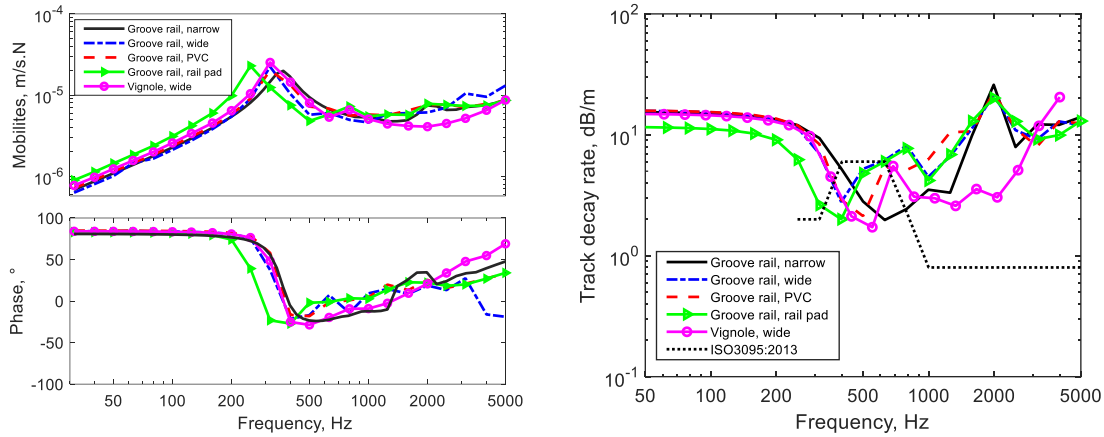

Figure 17. Comparison of dynamic properties of embedded track with narrow and wide filling. (a) Mobility magnitude; (b) track decay rate.

6.2 *Sound radiation of different tracks*

The sound power for a unit force, the mean-square velocity and the radiation efficiency of the different models are shown in Figure 18. The model with the soft rail pad has a higher vibration and radiated power at low frequencies due to its lower decay rate and higher mobility. However, the radiation efficiency is more similar to the other models in this frequency range. Above 300 Hz, where waves can propagate in the rail, this model gives almost identical results to the corresponding model without the rail pad, as their mobilities and decay rates are very similar. As seen above, embedding material has a greater effect on the decay rate than the relatively soft rail pad.

Compared with the narrow filling, all the models with the wide filling have a lower radiation efficiency above 500 Hz. However, their surface area is larger so the difference between the radiated power for the wide and narrow fillings is not so great. The three cases with the groove rail and wide filling each have a large dip in both the sound power and radiation efficiency between 630 and 1000 Hz. This will be explored in more detail below. The sound power radiated by the Vignole rail is higher than that from the other models between 500 and 1250 Hz. Compared with the groove rail with the wide filling, this difference in radiated power is a consequence of the higher vibration of the Vignole rail due to its lower decay rate.

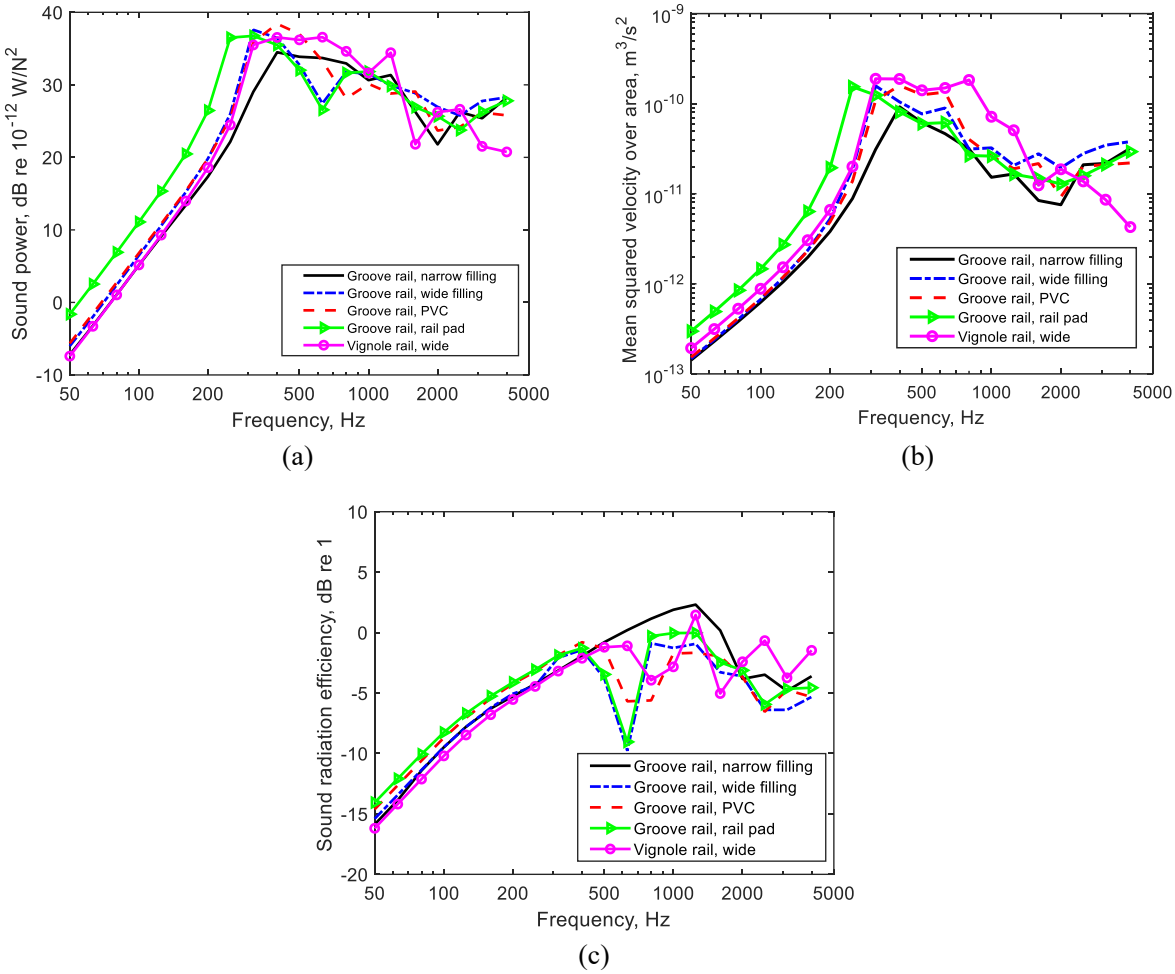

Figure 18. Comparison of sound radiation of embedded track with narrow and wide filling. (a) Sound power for a unit force; (b) mean squared velocity; (c) radiation efficiency.

Results are shown in Figure 19 to demonstrate the influence of the embedding material for the model shown in Figure 16(a), i.e. the groove rail with wide filling. Figure 19 shows the radiated sound power and radiation efficiency calculated from the vibration of the rail alone (i.e. by setting the velocity of the embedding material to zero in the BE calculation). These are compared with the results from Figure 18, which included the vibrating surface of the embedding material. Including the effect of the embedding material increases the sound power at most frequencies. The radiation efficiency is also increased at low frequencies as a consequence of the wider radiating area. However, it is reduced above 400 Hz. In this frequency region the vibration of the rubber surface becomes out of phase with the rail head. This is illustrated in Figure 20, which shows the wave shape associated with the predominantly vertical bending wave of the rail at about 630 Hz. Consequently, at this frequency the vibration of the embedding material causes some cancellation of the sound radiation from the rail; this is the

reason for the dip seen in Figure 19 at 630 Hz for this model.

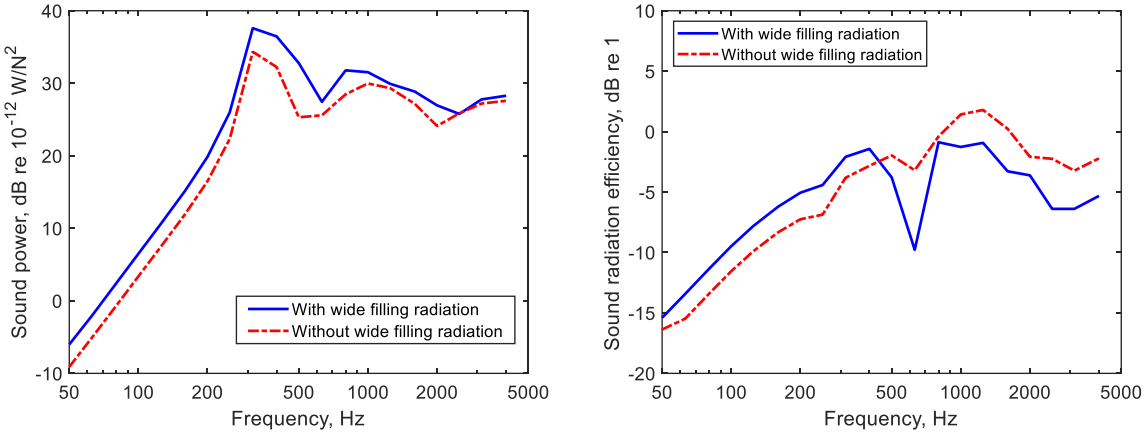

(a) (b)

Figure 19. Sound radiation of rail with and without radiation from the embedding material, for the groove rail with wide filling. (a) Sound power for a unit force; (b) radiation efficiency.

Figure 20. Wave shape of vertical bending of groove rail with wide filling at 630 Hz and wavenumber 4.7 rad/m.

6.3 *Comparison of rolling noise from embedded tracks*

To compare the rolling noise from the different track models, the sound pressure levels at 7.5 m from the track centreline are calculated using the same wheel model as in Section 5. In order to avoid strong influences of the roughness spectrum, the ISO 3095:2013 [20] reference curve is used as the input, again including the DPRS contact filter. The tram speed is taken as 56 km/h as before. Figure 21(a) shows the calculated A-weighted sound pressure spectra due to the track vibration and Figure 21(b) shows the total noise including the wheel contribution. The overall A-weighted noise levels and the contributions from the track and wheel are listed in Table 3. The wheel noise component is largely unaffected by the track design and, in terms of overall level, it is 6-8 dB(A) lower than the track noise component.

Table 3. A-weighted sound pressure levels at 7.5 m from track centreline for different embedded rail designs based on ISO 3095:2013 roughness spectrum at 56 km/h

Track type	Total noise (dBA)	Track noise (dBA)	Wheel noise (dBA)
Groove rail, narrow filling	60.2	59.5	51.8
Groove rail, wide filling	59.7	58.9	52.1
Groove rail, with PVC pipe	60.9	60.3	52.2
Groove rail, with rail pad	60.3	59.6	51.8
Vignole rail, wide filling	62.6	62.2	51.5

Although the embedded rail models with the wide filling have a larger radiating area than the narrow one, the noise levels of the models with wide and narrow filling are similar. This is due to the cancellation effects noted in the previous section. As already seen in Figure 18, the soft rail pad increases the track noise below 400 Hz because of the increased rail vibration, but above this frequency it has no effect. Apart from this case, the main differences between the various track models occur above 250 Hz. The Vignole rail has a higher noise level than the corresponding model with the groove rail between 300 and 1250 Hz due to its lower track decay rate. Its overall noise level is therefore the highest, about 3 dB greater than the groove rail with wide embedding. However, although its decay rate is also much lower than the others between 1600 and 2500 Hz, the noise radiation is not significantly different in this frequency region due to cancellation effects from the rubber. Introducing the PVC pipe leads to an increase of around 1 dB in the overall noise level; the level increases at 500 and 630 Hz but reduces slightly at 800 and 1000 Hz. These effects are caused by the differences in track decay rate (Figure 17(b)) and also the shift in the dip in the radiation efficiency (Figure 18(b)). In all cases a dip appears in the 800 Hz band. This occurs due to the strong resonance of the wheel in the radial direction at about 900 Hz, see Figure 12(a), which leads to a reduction in the wheel/rail force.

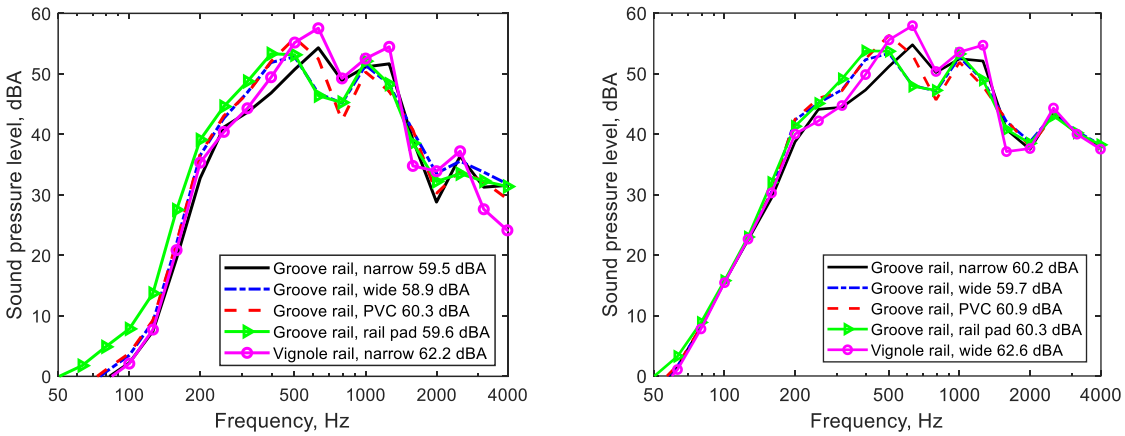

(a) (b)

Figure 21. A-weighted sound pressure levels at 7.5 m from track centreline for different embedded rail designs based on ISO 3095:2013 roughness spectrum at 56 km/h. (a) Track noise; (b) total noise.

7. Conclusions

A wavenumber domain (2.5D) numerical model for predicting the noise from embedded tracks has been presented, which includes the rail geometry, elastomeric embedding material, concrete structure, supporting soil stiffness and acoustic properties of the ground surface. The model is applied first to a track embedded in a grassy ground for which field measurements have been carried out. The predictions show good agreement with the measured point mobility and track decay rate. The vertical decay rate of this embedded grass track is quite low between 400 Hz and 1000 Hz, which results in high levels of rolling noise in this important frequency range. The concrete around the embedded rail vibrates strongly and radiates noise, particularly below 200 Hz, but it gives some cancellation of the radiation from the rail around 400 Hz where it vibrates out of phase with the rail. At higher frequencies it can be neglected. The absorptive effect of the grass tends to reduce the radiated noise over the whole frequency range, with differences of up to 2 dB in sound power. In addition the attenuation effect of the fairings around the bogie region is estimated taking account of the absorptive effect of the grass surface.

The rolling noise of this grass track is compared with field measurements and good agreement is observed. The rail contribution is shown to be dominant for frequencies between 300 and 1600 Hz. The noise contribution from the resilient wheels of the tramcar is relatively low compared with the track but the wheel contributes most of the noise at frequencies above

2 kHz.

Different designs of embedded rail are compared in terms of their vibration response and sound radiation. An embedding material with a wide surface can increase the track decay rate of the groove rail between 300 Hz and 1600 Hz. Although the embedded rail models with the wider filling have a larger radiating area than the narrow one, their noise levels are similar, at least for similar values of support stiffness as considered here. This is due to cancellation effects occurring at frequencies between 630 and 1000 Hz where the rubber vibrates out of phase with the rail. Including a soft rail pad beneath the rail foot increases the track noise at low frequency because of increased rail vibration, but above 400 Hz it has no effect on the track decay rates or the radiated noise. Replacing the groove rail by a Vignole rail leads to a lower track decay rate and consequently a higher noise level between 300 Hz and 1250 Hz. Its overall noise level is therefore the highest of those considered, about 3 dB greater than the corresponding track with the groove rail. Introducing a PVC pipe within the embedding material leads to an increase of around 1 dB in the overall noise level.

It is clear that the noise levels from an embedded rail depend on the details of the design and the material properties of the embedding material. Of particular importance is the frequency range for which cancellation occurs between the sound radiation from the rail and the embedding material. Consequently, mitigation measures for embedded track should be considered carefully on a case-by-case basis using models such as those presented here.

Acknowledgements

The work described here has been supported by the EPSRC under the programme grant EP/M025276/1, 'The science and analytical tools to design long life, low noise railway track systems (Track to the Future)'. This work was carried out while the first author was an academic visitor at ISVR, University of Southampton, sponsored by the CSC Program of China. The authors are grateful to Transport Infrastructure Ireland and especially to Stephen Byrne for assistance in the field tests. All data published in this paper are openly available from the University of Southampton repository at: https://doi.org/10.5258/SOTON/D1373.

References

[1] D.J. Thompson. Railway Noise and Vibration: Mechanisms, Modelling and Means of Control. Elsevier: Oxford, 2009.

[2] S. Sandrock, B. Griefahn, T. Kaczmarek, H. Hafke, A. Preis, T. Gjestland. Experimental studies on annoyance caused by noises from trams and buses. J. Sound Vib. 313.3-5(2008) 908-919.

[3] M. Cik, P. Lercher. Analysis of increased annoyance reactions after the introduction of new tramways, based on psychoacoustic parameters. In INTER-NOISE and NOISE-CON Congress and Conference Proceedings, 253(6)1987-1997. Institute of Noise Control Engineering, 2016.

[4] M.H.A. Janssens, M.G. Dittrich, F.G. De Beer, et al. Railway noise measurement method for pass-by noise, total effective roughness, transfer functions and track spatial decay. J. Sound Vib. 293.3-5(2006), 1007-1028.

[5] S.L. Grassie. Rail irregularities, corrugation and acoustic roughness: characteristics, significance and effects of reprofiling. Proc. Inst. Mech. Eng. Part F-J. Rail Rapid Transit. 226(2012) 542-557.

[6] L. Chiacchiari, D.J. Thompson, G. Squicciarini, E. Ntotsios, et al. Rail roughness and rolling noise in tramways. J. Phys. Con. Series 744(2016) 012147.

[7] P. Remington, J. Webb, Estimation of wheel/rail interaction forces in the contact area due to roughness. J. Sound Vib. 193(1996), 83-102.

[8] D.J. Thompson, B. Hemsworth, N. Vincent. Experimental validation of the TWINS prediction program for rolling noise, part 1: description of the model and method. J. Sound Vib. 193(1996), 123-135.

[9] M.A. Pallas, J. Lelong, R. Chatagnon. Characterisation of tram noise emission and contribution of the noise sources. Appl. Acoust. 72(2011), 437-450.

[10] S. Van Lier. The vibro-acoustic modelling of slab track with embedded rails. J. Sound Vib. 231(2000), 805-817.

[11] C.M. Nilsson, C.J.C. Jones, D.J. Thompson, J. Ryue. A waveguide finite element and boundary element approach to calculating the sound radiated by railway and tram rails. J. Sound Vib. 321(2009)813-36.

[12] Y. Zhao, X. Li, Q. Lv, H. Jiao, X. Xiao, X, Jin. Measuring, modelling and optimising an embedded rail track. Appl. Acoust. 116(2017) 70-81.

[13] X. Zhang, G. Squicciarini, D.J. Thompson. Sound radiation of a railway rail in close proximity to the ground. J. Sound Vib. 362(2016) 111-124.

[14] J. Ryue, S. Jang, D. J. Thompson. A wavenumber domain numerical analysis of rail noise including the surface impedance of the ground. J. Sound Vib. 432 (2018) 173-191.

[15] C.J.C. Jones, D.J. Thompson. Rolling noise generated by railway wheels with visco-elastic layers. J. Sound Vib. 231(2000), 779-790.

[16] P. Bouvet, N. Vincent, A. Coblentz, et al. Optimization of resilient wheels for rolling noise control. J. Sound Vib. 231(2000), 765-777.

[17] X. Sheng, C.J.C. Jones, D.J. Thompson. Modelling ground vibration from railways using wavenumber finite-and boundary-element methods. Proc. R. Soc. A-Math. Phys. Eng. Sci. 461.2059 (2005): 2043-2070.

[18] C.M. Nilsson, C.J.C. Jones. Theory manual for WANDS 2.1 wave number domain FE-BE

software for structures and fluids, 2007.
[19] EN 15461:2008+A1:2010: Railway applications - Noise emission - characterization of the dynamic properties of track selections for pass by noise measurements, 2010, European Committee for Standardization, Brussels.
[20] ISO 3095:2013. Acoustics–railway applications–measurement of noise emitted by railbound vehicles. International Standards Organization, Geneva, 2013.
[21] M.E. Delany, E.N. Bazley, Acoustical properties of fibrous absorbent materials, Appl. Acoust. 3 (1970) 105–116.
[22] T.F.W, Embleton, J.E. Piercy, G.A. Daigle. Effective flow resistivity of ground surfaces determined by acoustical measurements. J. Acoust. Soc. Am. 74(1983): 1239-1244.
[23] D.J. Thompson, Wheel-rail noise generation, part I: introduction and interaction model. J. Sound Vib. 161(1993), 387-400.
[24] E.T. Paris, On the reflexion of sound from a porous surface. Proc. R. Soc. London Ser. A-Math. 115.771 (1927) 407-419.
[25] F. Fahy, D. Thompson (eds). Fundamentals of Sound and Vibration, 2nd edition. CRC press, Boca Raton, 2015.